Separated two-phase flow model of cryogenic loading operation

Dmitry G Luchinskiy[1], Ekaterina Ponizovskaya-Devine[2], Michael Khasin[3], Dogan Timucin[4], Jarred Sass[5], Jose Perotti[6], Barbara Brown[7]

[1,2] *Mission Critical Technologies, Inc., El Segundo, CA, 94035, USA*
dmitry.g.luchinsky@nasa.gov

[2,3] *SGT, Inc., Greenbelt, MD, USA*
ekaterina.v.ponizovskayadevine@nasa.gov
michael.khasin@nasa.gov

[4] *NASA Ames Research Center, Moffett Field, CA, 94035, USA*
dogan.timucin@nasa.gov

[5,6,7] *Kennedy Space Center, Kennedy Space Center, FL, 32899, USA*
jose.m.perotti@nasa.gov
jared.p.sass@nasa.gov
barbara.l.brown@nasa.gov

Abstract

We present results of development of separated two-phase cryogenic flow model motivated by NASA plans to mature technology of autonomous cryogenic management on the ground and in space. The solution algorithm is based on the nearly-implicit scheme. We discuss the stability, speed, and accuracy of the algorithm in the context of applications to on-line health management of cryogenic loading operation. We present the results of validation of the model by comparison with the experimental data obtained during chilldown of the horizontal transfer line obtained at National Bureau of Standards and at the cryogenic testbed in Kennedy Space Center. We demonstrate a good agreement of the model predictions with the experimental data.

1. Introduction

Modeling boiling two-phase flow is of great interest to many aerospace applications (Konishi & Mudawar, 2015). Fast, time-accurate predictions of cryogenic two-phase flow are especially important for autonomous control of cryogenic propellant loading on the ground and in space (Robert, William, Kelly, & Evelyn, 2012).

Predicting the dynamics of boiling two-phase flows is a long standing challenging problem (Prosperetti & Tryggvason, 2007; Ishii & Hibiki, 2010). The problem becomes even more complicated when analysis of the cryogenic flow is required under reduced gravity conditions, because there is a severe shortage of useful correlations (Konishi & Mudawar, 2015).

At the same time a number of efficient algorithms (TRACE5, 2007; RELAP5:1, 2012; Nourgaliev & Christon, 2012; Berry et al., 2014) and advanced correlation relations (Choi et al., 2009; RELAP5:4, 2012) for analysis of multi-phase flows have been developed during recent years. It is of great interest to verify if the current state of art techniques in modeling multiphase flows can be effectively applied to the on-line control and integrated health management of cryogenic loading operations.

Here we present the results of development of separated two-phase flow model of cryogenic flow in transfer line using nearly implicit algorithm (RELAP5:1, 2012). We provide details of the algorithm and discuss the stability, speed, and accuracy. We present results of verification and validation of the model using two sets of experimental data obtained during chilldown of the cryogenic transfer line at National Bureau of Standards and at Kennedy Space Center. In conclusions, we summarize obtained results, briefly outline future work and discuss possible applications.

Dmitry Luchinsky et al. This is an open-access article distributed under the terms of the Creative Commons Attribution 3.0 United States License, which permits unrestricted use, distribution, and reproduction in any medium, provided the original author and source are credited.

2. MODEL

We model cryogenic loading and chilldown using Wallis equations (Wallis, 1969) for a one-dimensional separated two-phase flow. The model consists of a set of conservation laws for the mass, momentum, and energy for the gas

$$\begin{aligned}
&(\alpha\rho_g)_{,t} + \tfrac{1}{A}(A\alpha\rho_g u_g)_{,x} = \Gamma_g \\
&(\alpha\rho_g u_g)_{,t} + \tfrac{1}{A}\left(A\alpha\rho_g u_g^2\right)_{,x} + \alpha p_{,x} = -\alpha\rho_g \sin\theta \\
&\quad -\tau_{wg}\tfrac{l_{wg}}{A} - \tau_{ig}\tfrac{l_i}{A} + \Gamma_g u_{ig} \\
&(\alpha\rho_g e_g)_{,t} + \tfrac{1}{A}(A\alpha\rho_g e_g u_g)_{,x} = -\tfrac{1}{A}(pA\alpha u_g+)_{,x} \\
&\quad -p\alpha_{,t} + \dot{q}_{wg}\tfrac{l_{wg}}{A} + \dot{q}_{ig}\tfrac{l_i}{A} + \Gamma_{ig}h_{ig} + \Gamma_{wg}h_{wg}
\end{aligned} \tag{1}$$

and for the liquid

$$\begin{aligned}
&(\beta\rho_l)_{,t} + \tfrac{1}{A}(A\beta\rho_l u_l)_{,x} = -\Gamma_g \\
&(\beta\rho_l u_l)_{,t} + \tfrac{1}{A}\left(A\beta\rho_l u_l^2\right)_{,x} + \beta p_{,x} = -\beta\rho_l \sin\theta - \\
&\quad \tau_{wl}\tfrac{l_{wl}}{A} - \tau_{il} l_i - \Gamma_g u_{il} \\
&(\beta e_l\rho_l)_{,t} + \tfrac{1}{A}(A\beta e_l\rho_l u_l)_{,x} = -\tfrac{1}{A}(pA\beta u_l)_{,x} + \\
&\quad -p\beta_{,t} + \dot{q}_{wl}\tfrac{l_{wl}}{A} + \dot{q}_{li}\tfrac{l_i}{A} - \Gamma_{ig}h_{ig} - \Gamma_{wg}h_{wg}
\end{aligned} \tag{2}$$

coupled to the equation for the wall temperature

$$\begin{aligned}
\rho_w c_w d_w \frac{\partial T_w}{\partial t} &= H_{wg}\left(T_g - T_w\right) + \\
&H_{wl}\left(T_l - T_w\right) + H_{amb}\left(T_{amb} - T_w\right).
\end{aligned} \tag{3}$$

Each phase of the fluid is characterized by its own void fraction α_k, density ρ_k, temperature T_k (energy e_k), and velocity u_k, where index k takes values g for the gas/vapor phase and l for liquid phase. A closed system of equations can be obtained assuming local pressure values for the two phases are equal ($p_g = p_l = p$) and that the source terms on the right-hand sides of the balance equations are exclusive algebraic functions of state and flow parameters. In addition, each phase is characterized by the mass flow rate Γ_g (negative for the liquid), heat flux to the dry wall (q_{gw}) and to the wetted wall (q_{lw}), heat flux at the interfaces ($q_{(g(l)i)}$), pressure losses at the dry and wetted wall ($\tau_{(g(l)w)}$) and at the interface (τ_{li}), and relative velocity at the interface (u_{il}). The geometry of the sections is determined by the length L of the section, cross-section area (A), height (y), wetted (l_{wl}), dry (l_{wg}), and interface (l_i) perimeters.

The heat transfer to the wall is characterized by the heat transfer coefficient from gas (liquid) to the wall $H_{g(l)w}$ and the heat transfer coefficient from the environment to the wall H_{amb}. $T_{g(l)}$ is the temperature of the gas (liquid), and ρ_w, c_w, and A_w are wall material density, specific heat, and cross-section area.

The set of equations (1) - (3) is closed by the volume conservation condition and equations of state

$$\alpha_g + \alpha_l = 1, \qquad \rho_{(g,l)} = \rho_{(g,l)}\left(p, e_{(g,l)}\right) .$$

We tested a number of algorithms that solve equations (1) - (3) in various approximations (Luchinsky, Smelyanskiy, & Brown, 2014a, 2014c; Hafiychuk et al., 2014). Here we present details of the nearly implicit algorithm, which was developed following closely the ideas of (RELAP5:1, 2012), and delivers one of the best performance in terms of speed, level of details, and accuracy.

3. ALGORITHM

The calculations of the velocities, pressure, and provisional values of densities and energies at the first sub-step of the algorithm is the key to the stable performance of the nearly-implicit method. These calculations are designed to break limitations of the acoustic and material CFL and to increase implicitness of the method. This sub-step is structured as a predictor of the fractional time step technique. The CFL limitations are lifted by increased implicitness of calculations of the new velocities and pressures in the system. The implicitness is further increased by estimations of the provisional values of the densities, energies, heat and mass transfer coefficients.

The first step of the algorithm can be briefly summarized as follows:

- Solve expanded equation with respect to pressure in terms of new velocities;
- Solve momenta equations written in the form of block tri-diagonal matrix for the new velocities;
- Find new pressure;
- Find provisional values for energies and void fractions using expanded equations;
- Find provisional values of mass fluxes and heat transfer coefficients using provisional values of temperatures obtained.

At the second step new (corrected) values of the densities, void fractions, and energies are found by solving the unexpanded conservation equations for the phasic masses and energies using provisional values for the heat and mass fluxes in source terms. The solution is reduced to independent solution of four tri-diagonal matrices. The values of pressure and velocities in these matrices are taken at the new time step.

We now provide some further details of the algorithm.

3.1. First step of the algorithm

To find new pressure we first express it in terms of new velocities. To do so we formally solve the following set of expanded conservation equations discretized on the main grid (the notation convention for the grid is shown in Fig. 1)

The sum density equation

$$\begin{aligned}&\alpha^n_{g,L} d\rho^{n+1}_{g,L} + \beta^n_{l,L} d\rho^{n+1}_{l,L} + d\alpha^{n+1}_{g,L} \left(\rho_g - \rho_l\right)^n_L + \\ &\Delta t \left(\left(\overline{\alpha\rho}\right)^n_{g,j+1} \eta^{n+1}_{g,j+1} - \left(\overline{\alpha\rho}\right)^n_{g,j} \eta^{n+1}_{g,j} \right) + \\ &\Delta t \left(\left(\overline{\alpha\rho}\right)^n_{l,j+1} \eta^{n+1}_{l,j+1} - \left(\overline{\alpha\rho}\right)^n_{l,j} \eta^{n+1}_{l,j} \right) = 0.\end{aligned} \tag{4}$$

The difference density equation

$$\begin{aligned}&\alpha^n_{g,L} d\rho^{n+1}_{g,L} - \beta^n_{l,L} d\rho^{n+1}_{l,L} + d\alpha^{n+1}_{g,L} \left(\rho_g + \rho_l\right)^n_L + \\ &\Delta t \left(\left(\overline{\alpha\rho}\right)^n_{g,j+1} \eta^{n+1}_{g,j+1} - \left(\overline{\alpha\rho}\right)^n_{g,j} \eta^{n+1}_{g,j} \right) - \\ &\Delta t \left(\left(\overline{\alpha\rho}\right)^n_{l,j+1} \eta^{n+1}_{l,j+1} - \left(\overline{\alpha\rho}\right)^n_{l,j} \eta^{n+1}_{l,j} \right) = 2\Gamma^n_{g,L}.\end{aligned} \tag{5}$$

The gas energy equation

$$\begin{aligned}&\left(\rho_g e_g + p\right)^n_L d\alpha^{n+1}_{g,L} + \left(\alpha\rho\right)^n_{g,L} de^{n+1}_{g,L} + \\ &\left(\alpha e\right)^n_{g,L} d\rho^{n+1}_{g,L} + \quad \Delta t \left[\left(\bar{\alpha}\left(\overline{\rho e} + p\right)\right)^n_{g,j+1} \eta^{n+1}_{g,j+1} + \right. \\ &\left. \left(\bar{\alpha}\left(\overline{\rho e} + p\right)\right)^n_{g,j} \eta^{n+1}_{g,j} \right] = \left[H^n_{gw} \left(T^n_w - \tilde{T}^{n+1}_g \right)_L S_{wg} \right. \\ &+ H^n_{ig} \left(\tilde{T}^{n+1}_{s,l} - \tilde{T}^{n+1}_g \right)_L S_{ig} \\ &\left. + \tilde{\Gamma}^n_{ig,L} h^n_{ig,L} + \tilde{\Gamma}^n_{wg,L} h^n_{wg,L} \right] \frac{\Delta t}{V},\end{aligned} \tag{6}$$

and the liquid energy equation

$$\begin{aligned}&-\left(\rho_l e_l + p\right)^n_L d\alpha^{n+1}_{g,L} + \left(\alpha\rho\right)^n_{l,L} de^{n+1}_{l,L} + \\ &\left(\alpha e\right)^n_{l,L} d\rho^{n+1}_{l,L} + \Delta t \left[\left(\bar{\alpha}\left(\overline{\rho e} + p\right)\right)^n_{l,j+1} \eta^{n+1}_{l,j+1} + \right. \\ &\left. \left(\bar{\alpha}\left(\overline{\rho e} + p\right)\right)^n_{l,j} \eta^{n+1}_{l,j} \right] = \left[H^n_{lw} \left(T^n_w - \tilde{T}^{n+1}_l \right)_L S_{wl} \right. \\ &+ H^n_{il} \left(\tilde{T}^{n+1}_{s,l} - \tilde{T}^{n+1}_l \right)_L S_{il} \\ &\left. - \tilde{\Gamma}^n_{ig,L} h^n_{il,L} - \tilde{\Gamma}^n_{wg,L} h^n_{wl,L} \right] \frac{\Delta t}{V}.\end{aligned} \tag{7}$$

Here $\eta^{n+1}_{g(l),j} = A_j u^{n+1}_{g(l),j} / V_L$.

Using the following expansion for the densities

$$\begin{aligned}d\rho^{n+1}_{g,L} &\approx \left(\frac{\partial\rho}{\partial p}\right)^n_{g,L} dp^{n+1}_L + \left(\frac{\partial\rho}{\partial e}\right)^n_{g,L} de^{n+1}_{g,L}; \\ d\rho^{n+1}_{l,L} &\approx \left(\frac{\partial\rho}{\partial p}\right)^n_{l,L} dp^{n+1}_L + \left(\frac{\partial\rho}{\partial e}\right)^n_{l,L} de^{n+1}_{l,L};\end{aligned}$$

and keeping temperatures at the previous time step the equations (4) – (7) can be written in the matrix form as follows

$$\begin{aligned}A^n_x \begin{bmatrix} d\alpha_g \\ de_g \\ de_l \\ dp \end{bmatrix}^{n+1}_L &= a^n_x du^{n+1}_{g,j+1} + \\ b^n_x du^{n+1}_{g,j} + c^n_x du^{n+1}_{l,j+1} &+ d^n_x du^{n+1}_{l,j} + e^n_x,\end{aligned} \tag{8}$$

The matrix and vector elements in equation (8) are defined in Appendix A.

By solving (8) for dp^{n+1}_L we have

$$\begin{aligned}dp^{n+1}_L = \left(A^n_x\right)^{-1}_4 &\left(a^n_x du^{n+1}_{g,j+1} + b^n_x du^{n+1}_{g,j} + \right. \\ &\left. c^n_x du^{n+1}_{l,j+1} + d^n_x du^{n+1}_{l,j} + e^n_x \right)\end{aligned} \tag{9}$$

where $\left(A^n_x\right)^{-1}_4$ is the 4-th row of the inverted matrix A_x.

By using (9) to eliminate new pressure from momenta equations we obtain block tri-diagonal matrix equation for the new velocities in the form

$$\begin{bmatrix} B_1 & C_1 & & \\ A_2 & B_2 & C_2 & \\ \ddots & \ddots & & \ddots \\ \dots & \dots & A_N & B_N \end{bmatrix} \begin{bmatrix} x_1 \\ x_2 \\ \vdots \\ x_N \end{bmatrix} = \begin{bmatrix} k_1 \\ k_2 \\ \vdots \\ k_N \end{bmatrix} \tag{10}$$

where coefficients of 2×2 matrices A, B, and C and vectors $x_m = \left[du^{n+1}_{g,m}, du^{n+1}_{l,m} \right]^T$ and $k_m = \left[n^n_{2m-1}, n^n_{2m} \right]^T$ are given in Appendix B.

3.2. Second step

The new velocities and pressure and provisional values for the temperatures can be substituted into unexpanded equations of the mass and energy conservations (first and last equations in (1) and (2), see (RELAP5:1, 2012) for further details). All four equations can be re-written in the standard tridiagonal form

$$a_L dU^{n+1}_{L-1} + b_L dU^{n+1}_L + c_L dU^{n+1}_{L+1} = S_L, \tag{11}$$

and solved efficiently using standard solvers. The explicit form of the conservative terms dU^{n+1}_L, source terms S_L, and matrix coefficients $a_L = -\lambda^{n+1}_j \gamma^{n+1}_j$, $b_L = 1 + \lambda^{n+1}_{j+1} \gamma^{n+1}_{j+1} - \mu^{n+1}_j \gamma^{n+1}_j$, and $c_L = \mu^{n+1}_{j+1} \gamma^{n+1}_{j+1}$ is given in Appendix C.

The structure of these terms is clear from the equations (1) and (2). Here we provide as an example the structure of the S_L term for the first equation (1)

$$S_{g,L} = \frac{\tilde{\Gamma}^n_{g,L} \Delta t}{V_L} - \left(\alpha\rho\right)^n_{g,j+1} \gamma^{n+1}_{g,j+1} + \left(\alpha\rho\right)^n_{g,j} \gamma^{n+1}_{g,j}. \tag{12}$$

Note that coefficients a_L, b_L, and c_L for the tridiagonal matrix are the same for each pair of density and energy equations.

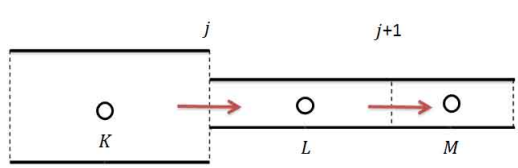

Figure 1. The notation convention for the centers of the control volumes on the main and staggered grid.

Calculation of the updated densities, void fractions, and energies completes the time step of integration of the semi-implicit algorithm.

3.3. Correlations

The thermodynamic properties of the cryogenic flow are modeled using multiple correlations for the source terms. The heat transfer and pressure losses correlations are based on the flow pattern recognition. Currently we are using the flow map introduced for refrigerants by Wojtan et al (Wojtan, Ursenbacher, & Thome, 2005). It is a modification of the map by Kattan et al (Kattan, Thome, & Favrat, 1998) and it is based on the Steiner map (Steiner & Kind, 2010). The latter map determines transitions between flow regimes as a relation between fundamental hydrodynamic numbers and geometrical parameters of the flow.

The two-phase friction pressure drop $\left(\frac{dp}{dz}\right)_{2\phi}$ is defined using Lockhart-Martinelli correlations (Chisholm, 1967). The pressure losses between the phases are partitioned (RELAP5:1, 2012) as follows

$$\tau_{wg} l_{wg} = \alpha_g \left(\frac{dp}{dz}\right)_{2\phi} \left(\frac{1}{\alpha_g + \alpha_l Z^2}\right),$$
$$\tau_{wl} l_{wl} = \alpha_l \left(\frac{dp}{dz}\right)_{2\phi} \left(\frac{Z^2}{\alpha_g + \alpha_l Z^2}\right).$$

Here Z^2 is given by

$$Z^2 = \left(f_l Re_l \rho_l u_l^2 \frac{\alpha_{wl}}{\alpha_l}\right) \Big/ \left(f_g Re_g \rho_g u_g^2 \frac{\alpha_{wg}}{\alpha_g}\right).,$$

friction factor $f_{g(l)}$ is approximated using Churchill formula (Churchill, 1977). Coefficients α_{wl} and α_{wg} depend on the flow pattern (RELAP5:1, 2012).

The interface drag is given by

$$\tau_{ig} = -\tau_{il} = \frac{1}{2} C_D \rho_g \left|u_g - u_l\right| \left(u_g - u_l\right),$$

where interfacial drag coefficient C_D depends on the flow pattern (TRACE5, 2007).

The heat transfer correlations are subject of extensive research (Tong & Tang, 1997; Faghri & Zhang, 2006) and will be considered in more details elsewhere. Here we briefly outline the framework for the development of the correlation module. The heat fluxes at the wall and at the interface are defined as follows

$$\dot{q}_{wg} = H_{wg}\left(T_w - \tilde{T}_g\right); \quad \dot{q}_{ig} = H_{ig}\left(\tilde{T}_{l,s} - \tilde{T}_g\right);$$
$$\dot{q}_{wl} = H_{wl}\left(T_w - \tilde{T}_l\right); \quad \dot{q}_{il} = H_{il}\left(\tilde{T}_{l,s} - \tilde{T}_l\right).$$

Here the heat transfer coefficients $H_{wg(l)}$ and $H_{ig(l)}$ have to be defined for each flow regime.

The total interfacial mass flux per unit volume $\Gamma_g = \Gamma_{wg} + \Gamma_{ig}$ in equations (1) and (2) are defined in terms of the heat fluxes as follows at the wall

$$\Gamma_{wg} = f_{cor} \frac{\dot{q}_{wl}}{h_g^* - h_l^*} \frac{l_{wl}}{A};$$

and at the interface

$$\Gamma_i = \frac{\dot{q}_{li} + \dot{q}_{gi}}{h_g^* - h_l^*} \frac{l_i}{A},$$

where the enthalpies are are given by the following expression

$$h_g^* - h_l^* = \begin{cases} h_{g,s} - h_l, & \Gamma > 0 \\ h_g - h_{l,s}, & \Gamma < 0 \end{cases}.$$

The heat transfer coefficients $H_{wg(l)}$ and $H_{ig(l)}$ are defined using heat transfer correlations at the wall and at the interface that depend on the flow pattern, mass flow rate, and flow quality. For example, in the single phase flow the heat transfer is determined by the largest of four possible heat transfer coefficients corresponding to laminar and turbulent, forced and natural convection (see e.g. (TRACE5, 2007; Nellis & Klein, 2009; Holman, 1989)).

Another important example is the heat transfer correlations for the horizontally stratified flow that should recognize nucleate, transition, and film boiling regimes. At present the flow boiling correlations in horizontally stratified regime are defined as corrections to the pool boiling correlations. In this context the correlations are focused on the estimations of the onset of nucleate boiling, critical heat flux, and minimum film boiling parameters and corresponding corrections due to forced convection.

The onset of nucleate boiling is correlated using ideas of (Frost, Dzakowic, & American Society of Mechanical, 1967) (see also (Ghiaasiaan, 2008)). The critical heat flux is modelled using Griffith flow corrections (Griffith, 1975) to Zuber correlations (Zuber & Tribus, 1958). The onset of film boiling is estimated using Iloeje flow corrections (Iloeje, Plummer, Rohsenow, & Griffith, 1982) to Berenson correlations (Berenson, 1961). The correlations for two other regimes recognized by the present version of the present model include annular and mist flow and follow (TRACE5, 2007; RELAP5:4, 2012) in micro-gravity.

The ability to include the full range of correlations for the two-phase non-equilibrium boiling flow is an important advantage of the model especially in the view of the possible applications of the model to the autonomous control of cryogenic fluid management.

4. STABILITY AND SPEED

The resulting very efficient and fast computational scheme is a variation of the algorithm developed in (RELAP5:1, 2012). It involves inversion of N 4×4 matrices, solution

of $(N-1)$ tree-block-diagonal matrix equation, solution of four $N \times N$ tridiagonal matrix equations, and $N \times m$ explicit computations. The implicitness of the nearly-implicit scheme (RELAP5:1, 2012) is elevated to break both acoustic and material CFL (Nourgaliev & Christon, 2012), yet the algorithm resolves both types of waves and scales linearly with the number of control volumes.

However, a number of inherent instabilities can severely slow down computations and sometimes prevent the convergence of the scheme. Specifically, the basic Wallis (Wallis, 1969) model (1), (2) is known to be non-hyperbolic and stiff (Staedtke, 2006). It also lacks positivity and subject to the instabilities due to the phase appearance-disappearance (Nourgaliev & Christon, 2012; Cordier, Degond, & Kumbaro, 2014).

The non-hyperbolicity of the model is related to the existence of a pair of complex eigenvalues whenever $u_g \neq u_l$. It can be corrected using variety of the methods including e.g. addition of virtual mass term (RELAP5:1, 2012; Staedtke, 2006).

The stiffness of the model is related to the nature of the source terms and results in the set of eigenvalues for the 4×4 matrices A_x^n that may differ by twelve orders of magnitude. Numerical experience shows that codding explicit solution for the inverted 4×4 matrices at the first step of the algorithm can substantially improve its performance.

4.1. Lack of positivity

The lack of positivity and the phase appearance-disappearance problems could not be completely eliminated in the existing methods of solution. It is important to note that the corresponding instabilities are not related to the incomplete implicitness of the method and are sever even in fully implicit versions (Bestion, 2000). It is related to the fact that for small values of the volume fraction of the disappearing phase and for large enough time steps the mass fluxes related to the mass exchange between phases may exceed the quantity of the remaining mass.

To mitigate this problem limiters on the values of pressure and a time step control are introduced to the algorithm. The problem can also be partially mitigated by using smoothers discussed in the following section.

4.2. Phase appearance disappearance

The most significant stability issue is related to the phase appearance disappearance (Bestion, 2000; Nourgaliev & Christon, 2012; Cordier et al., 2014). Although both mathematical and physical roots of this instability are clearly established no general solution of the problem was proposed so far.

In the limit of vanishing volume fraction of one of the phases, the two phases almost decouple and the minority phase obeys a pressureless gas dynamics system (Cordier et al., 2014). The physical origin of this problem can be traced back to the large density perturbation due to gravitational instability (Zeldovich, 1970). (see (Bouchut, Jin, & Li, 2003)).

A more formal approach reveals that in the limit of vanishing phase this system becomes non-hyperbolic because the Jacobian of the flux matrix is not diagonalizable and most shock-capturing schemes, which require a complete basis of eigenvectors, breakdown in this limit (Cordier et al., 2014). Although no general satisfactory solution was found so far, the problem can be partially mitigated by using smoothing scheme following e.g. recommendations by Liou (Chang & Liou, 2007) and adjust temperature, velocity, and density according to the following expression

$$\phi_{adj} = g(x)\phi_d + (1 - g(x))\,\phi_c, \tag{13}$$

where

$$g(x) = x^2\,(2x-3)\,; \quad \text{and} \quad x = \frac{\alpha_d - x_{\min}}{x_{\max} - x_{\min}}.$$

Here "d" stands for disappearing phase and "c" for conducting phase. The values of the minimum and maximum void fraction, for which smoothing (13) is applied are established using numerical experimentation and set currently at the 1×10^{-7} and 1×10^{-2} respectively.

We note that discussion of the instability due to the lack of positivity in (Bestion, 2000) is related to density-energy coupling, while discussion of the singularity due to the phase disappearance in (Cordier et al., 2014) is related to the density-momentum coupling. In practice, both types of instabilities can be coupled to each other. An analysis shows that conditioning of the matrix A_x in the first step of the algorithm has significant impact on the overall performance of the nearly implicit scheme and its stability properties. The results of this analysis will be presented elsewhere.

5. VERIFICATION AND VALIDATION

In the view of possible applications of the algorithm to the online integrated health management of cryogenic systems the verification and validation (V&V) of the algorithm using a large set of experimental data becomes especially important. For the validation we are using experimental data obtained at National Bureau of Standards (Brennan, Brentari, & Smith, 1966) and at the experimental loading system at Kennedy Space Center (Robert et al., 2012). Below we present some results of the V&V, some additional information can be found in (Luchinsky, Smelyanskiy, & Brown, 2014b).

5.1. Loading system

The sketch of the model of the cryogenic loading system developed at KSC for testing autonomous regimes of operation is shown in Fig. 2. The system consists of the storage tank

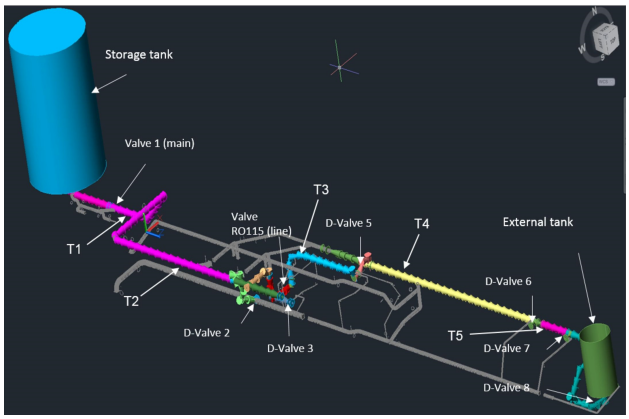

Figure 2. Sketch of the finite volume model of the system built in SINDA-FLUINT. Different colors correspond to the pipes of different diameters. Location of the main valves and sensors is indicated by arrows.

(left) and the external tank (right). The tanks are connected by a pipeline. A number of control valves and sensors can be seen along the loading path highlighted by colors. The location of the main input valve and of the pump are indicated in the figure. The cryogenic fluid is nitrogen. The characteristic speed of sound in the gas phase is about a_g = 200 m/sec and is about a_l = 700 m/sec in the liquid phase. The characteristic transient time of the pressure equilibration is less than 1 sec.

The system includes multiple control (damp) valves that remotely regulate flow during chilldown and loading. Temperature and pressure sensors located at several places along the system monitor the state of the flow. Importantly, the temperature of the flow is measured in the middle of the pipe. The real time accurate monitoring of complex nominal and off-nominal flow regimes during the loading and remote control of the flow by the valves make current system a unique and interesting experimental testbed well suited for the development of autonomous loading operations.

5.2. Pressure waves

The important feature of the nearly-implicit algorithm (RELAP5:1, 2012) is the ability to resolve both pressure and material waves. In this section we verify that the algorithm can resolve pressure wave propagation in the system.

To simplify the interpretation of the obtained results the following boundary conditions were specified. All the dump valves are closed. All the internal line control valves are opened. The pipes are initially filled with nitrogen gas at the temperature T =300K and pressure 1 atmosphere. The storage tank is filled with nitrogen gas at the same temperature. The pressure in the storage tank is 3.5 atm and in the vehicle tank 0.99 atm. The input and output valves are closed.

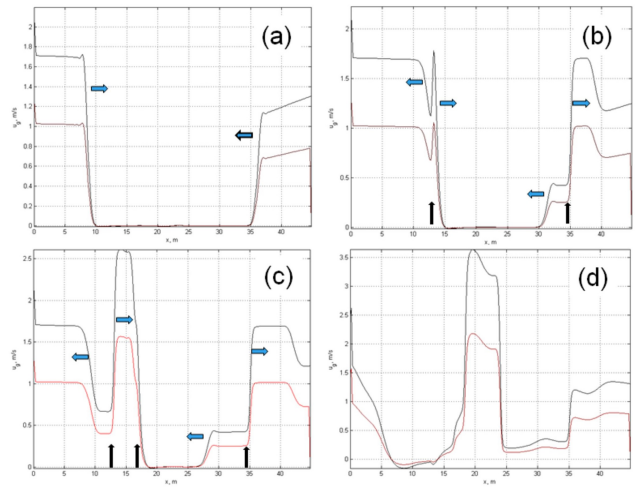

Figure 3. Propagation of the pressure waves. Snapshots are taken at: (a) 0.015 sec; (b) 0.01925 sec; (c) 0.02375 sec; and (d) 0.08125 sec. The directions on the waves propagation are indicated by blue wide arrows. The location of the transitions between pipes of different diameter are indicated by the vertical black arrows. The last snapshot shows nearly quasi-steady velocity distribution.

At the time instant $t = 0$ sec input and output valves are opened to 5 % of the their area allowing for a small shock wave propagation in the tube. The pressure in the shocks is less than 0.01 atm different as compared to the initial pressure in the pipes. These weak normal shock waves propagate in the pipes at nearly speed of sound.

The results of the integration of the model with 295 control volumes and time step Δt = 0.025 ms under given initial conditions are shown in the Fig. 3. The first snapshot taken at 0.0125 sec shows propagation of the shock waves away from the input and output valves towards the middle of the pipe. The velocities behind the shock waves on both sides of the system are positive because the pressure gradients on the input and output valves have the same direction. At the same time, the shock waves propagate in the opposite directions with velocity approximately 350 m/sec, which is very close to the speed of sound (a = 353 m/sec) in gaseous nitrogen at 300 K.

In the second snapshot taken at 0.01925 sec the wave front on the left encounters the transition from the 6 inch diameter pipe to the 3 inch diameter pipe at the distance approximately 12.5 m from the entrance. At this location the wave front splits and two waves: Transmitted wave continues to move forward, while reflected wave is propagating in the opposite direction.

Similar splitting occurs about 7 ms earlier at the location of another junction between the 2 inch and 4 inch pipes approximately 10 m away from the exit. Both locations and the direc-

tions of the wave propagation are indicated by black vertical arrows.

The third snapshot taken at 0.02375 sec shows how the wave front on the left is approaching the third junction located approximately 17 m from the entrance. This process continues until the velocity distribution in the pipe approaches quasi-equilibrium in approximately a few hundred milliseconds. The last snapshot (d) shows the nearly equilibrium distribution of the pressure in the pipe.

Examples of simulations of material waves can be found in (Luchinsky et al., 2014b). Below we provide two examples of validation of the algorithm.

5.3. Chilldown test by the National Bureau of Standards

The first example of the model validation is based on a well-known set of experimental data obtained for chilldown of horizontal transfer line at National Bureau of Standards (Brennan et al., 1966).

The vacuum jacketed line was 61 m long. The internal diameter of the copper pipe was 3/4 inches. Four measurement stations were located at the distance 6, 24, 42, and 60 m from the input valve. In the particular experiment, which was considered in this work the working liquid was nitrogen and pressure in the storage tank was 4.2 atm.

The comparison with the experimental data is shown in Fig. 4. The top figure shows model predictions for the fluid temperature as compared to the experimental time-traces. The bottom figure shows similar comparison for the wall temperature.

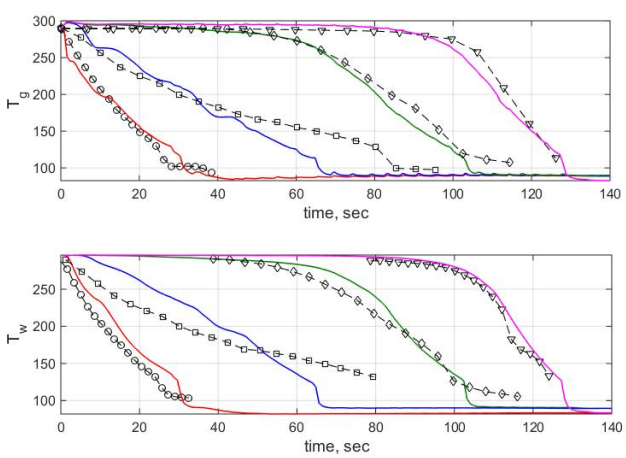

Figure 4. Model predictions (solid colored lines) for the fluid temperature (top) and wall temperature (bottom) are shown in comparison with the experimental time-traces (black dashed lines with open symbols) at 4 different locations along the transfer line: (i) 6 m from the line entrance (open circles); (ii) 24 m (open squares); (iii) 42 m (open diamonds); and (iv) 60 m (open triangles).

It can be seen from the figures that there are three different regions in the pipe. In the first region the pipe cools down to the liquid temperature in 30 sec and this part of the pipe is filled with liquid. In the second region the temperature is gradually changing towards liquid temperature during first 90 sec. In this region the dryout transition occurs. In the remaining part of the pipe the temperature stays high for a long period of time, indicating that the front of cold gas and the transition region are slowly moving along the pipe towards exit with the speed approximately 0.5 m/sec.

It can also be noticed from the figure that a sudden temperature drop occurs in the system whenever that fluid and wall temperature cool down to approximately 130 K. This temperature drop corresponds to the transition from the film boiling regime to the intermittent regime of boiling, when the heat transfer to the wall is sharply rising towards its maximum value, corresponding to the critical heat flux.

It can be seen from the figure that the model can reproduce all the experimentally observed features mentioned above. Further improvements of the model predictions in the transition region can be achieved by using more accurate correlations for various flow regimes as will be discussed in details elsewhere.

5.4. Chilldown cryogenic testbed

Our last example of the validation of the separated model is based on the comparison of the model predictions with the experimental time traces obtained during chilldown of the transfer line of the cryo-testbed at KSC. The schematics of the KSC cryo-testbed is shown in the Fig. 2.

There are two main features that differentiate this case from the previous example. Firstly, the complex geometry and a large number of components with minor losses and heat leaks render modeling of this system a challenging problem. Sec-

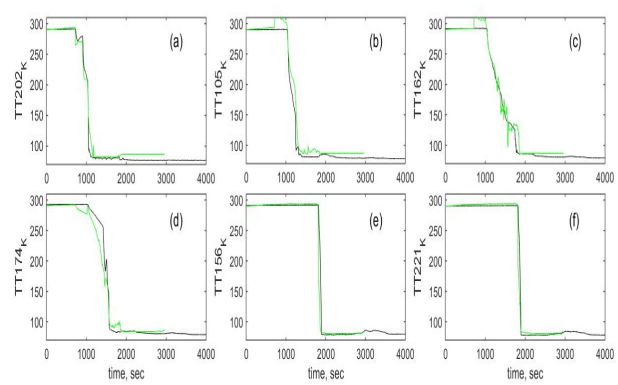

Figure 5. Model predictions (green lines) for the fluid temperature are shown in comparison with the experimental time-traces (black lines) at 6 different locations along the transfer line.

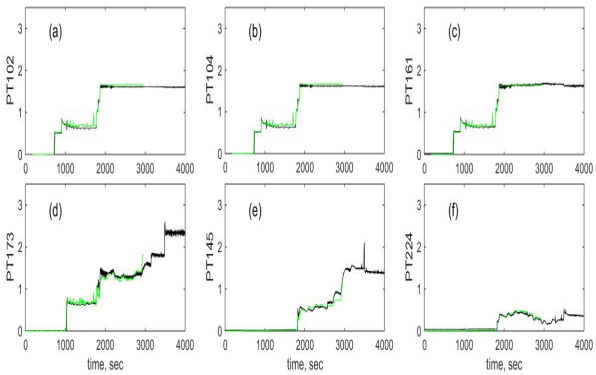

Figure 6. Model predictions (green lines) for the pressure in the pipes are shown in comparison with the experimental time-traces (black lines) at 6 different locations along the transfer line

ondly, the flow during chilldown is controlled by the bleed valves, in-line control valves, and by the storage tank pressure. As a results, the chilldown dynamics is very different from the previous case, where it was mainly controlled by the heat transfer from the boiling flow to the pipe walls.

The chilldown at the cryo-testbed was achieved in three steps (stages). Initially the input valve is open, allowing some liquid to flow into the hot pipes. This liquid immediately evaporates creating high pressure gas, blocking further liquid flow, and keeping the rest of the pipe hot. This stage can be recognized as a small deep in the fluid temperature in the Fig. 5 and the first pressure jump in the Fig. 6 (a), (b), and (c).

The second step begins when the second valve in the middle of the transfer line is opened. Simultaneously, a few bleed valves are opened creating enough suction for the cold flow to fill in half of the transfer line. This stage can be recognized by the temperature drop in Fig. 5 (a) - (d). Note, that the temperature remains high in the rest of the pipe until the end of this stage as can be seen in the Fig. 5 (e) and (f). One can also recognize this stage of chilldown by the pressure jump in Fig. 6 (d), while in the rest of the pipe the pressure stays low until the end of this stage (see Fig. 6 (e) and (f)).

The last chilldown step begins when the third line valve is open allowing the fluid to flow through the entire transfer line. This step can be identified as a fast temperature drop in Fig. 5 (e) and (f). It can also be seen as pressure jump in the Fig. 6 (e) and (f).

The comparison of the model predictions (green lines in the Fig. 5 and 6) with the experimental time traces (black lines) shows that the model can quite accurately reproduce all three stages of the chilldown. We note that the model integration is fast. The integration of nearly 3000 sec of real time shown in the figures takes several seconds on laptop.

6. CONCLUSION

To summarize we note that the developed separated model of the two-phase cryogenic flow allows for the fast and time accurate predictions of the chilldown dynamics in large scale systems with complex valve control. These capabilities of the model pave the way for its on-line applications to the integrated health management as will be discussed in details in a separate presentation.

We note also that the fast integration of the model using a variation of the nearly implicit algorithm (RELAP5:1, 2012) opens a possibility of development of a set of optimization tools that can be used to optimize the loading regimes and speed up the development and design of cryogenic transfer lines under normal and reduced gravity conditions. The development and testing of such optimization tools is currently under way and will be a subject of future presentations.

Importantly, the separated model allows one to incorporate and verify a wide range of correlations available for cryogenic boiling flows. Once the model is equipped with the set of optimization tools many of the unknown parameters of those correlations can be learned from the experimental data under various complex flow conditions required for the development of autonomous cryogenic loading operations in micro-gravity.

ACKNOWLEDGMENT

This work was supported by the Advanced Exploration Systems and Game Changing Development programs at NASA HQ.

NOMENCLATURE

u	velocity
T	temperature
p	pressure
e	specific energy
h	specific enthalpy
H	heat transfer coefficient
g	gravity
Re	Reynolds number
t	time
Δt	time step
A	cross-sectional area
S	wall surface area
V	volume of the control volume
l	perimeter
x	coordinate along the pipe
y	height of the control volume
$\dot{q}$	heat flux
c	specific heat

Greek	
α	gas void fraction
β	liquid void fraction
ρ	density
τ	wall shear stress
Γ	mass flux per unit volume
Subscript	
g	gas
l	liquid
w	wall
i	interface

REFERENCES

Berenson, P. (1961). Film-boiling heat transfer from a horizontal surface. *Journal of Heat Transfer*, *83*, 351–358.

Berry, R. A., Peterson, J. W., Zhang, H., Martineau, R. C., Zhao, H., Zou, L., & Andrs, D. (2014). Relap-7 theory manual [Computer software manual]. Idaho Falls, Idaho 83415.

Bestion, D. (2000, September). *The phase appearance and disappearance in the cathare code.* Trends in Numerical and Physical Modeling for Industrial Multiphase Flows.

Bouchut, F., Jin, S., & Li, X. (2003). Numerical approximations of pressureless and isothermal gas dynamics [Journal Article]. *SIAM Journal on Numerical Analysis*, *41*(1), 135-158.

Brennan, J. A., Brentari, E. G., & Smith, W. G., R. V.and Steward. (1966). *Cooldown of cryogenic transfer lines* (Technical Report No. NBS Report 9264). National Bureau of Standards.

Chang, C.-H., & Liou, M.-S. (2007). A robust and accurate approach to computing compressible multiphase flow: Stratified flow model and ausm+-up scheme. *Journal of Computational Physics*, *225*(1), 840 - 873.

Chisholm, D. (1967). A theoretical basis for the lockhart-martinelli correlation for two-phase flow [Journal Article]. *International Journal of Heat and Mass Transfer*, *10*(12), 1767-1778.

Choi, K. Y., Yun, B. J., Park, H. S., Kim, H. D., Kim, Y. S., Lee, K. Y., & Kim, K. D. (2009). Development of a wall-to-fluid heat transfer package for the space code [Journal Article]. *Nuclear Engineering and Technology*, *41*(9), 1143-1156.

Churchill, S. W. (1977). Friction-factor equation spans all fluid-flow regimes [Journal Article]. *Chemical Engineering*, *84*(24), 91-92.

Cordier, F., Degond, P., & Kumbaro, A. (2014). Phase appearance or disappearance in two-phase flows. *Journal of Scientific Computing*, *58*(1), 115-148.

Faghri, A., & Zhang, Y. (2006). *Transport phenomena in multiphase systems* [Book]. Elsevier Science.

Frost, W., Dzakowic, G. S., & American Society of Mechanical, E. (1967). *An extension of the method for predicting incipient boiling on commercially finished surfaces* [Book]. New York, N.Y.: ASME.

Ghiaasiaan, S. M. (2008). *Two-phase flow, boiling and condensation in conventional and miniature systems* [Book]. New York: Cambridge University Press.

Griffith, P. (1975). Counterflow critical heat flux. In *Aiche paper, symposium series* (Vol. 174). San Francisco: AIChE.

Hafiychuk, V., Foygel, M., Ponizovskaya-Devine, E., Smelyanskiy, V., Watson, M. D., Brown, B., & Goodrich, C. (2014). Moving-boundary model of cryogenic fuel loading, i: Two-phase flow in a pipe [Journal Article]. *Journal of Thermophysics and Heat Transfer*, 1-12.

Holman, J. P. (1989). *Heat transfer* [Book]. McGraw-Hill.

Iloeje, O. C., Plummer, D. N., Rohsenow, W. M., & Griffith, P. (1982). Effects of mass flux, flow quality, thermal and surface properties of materials on rewet of dispersed flow film boiling. *Journal of Heat Transfer*, *104*(2), 304-308.

Ishii, M., & Hibiki, T. (2010). *Thermo-fluid dynamics of two-phase flow*. Bcher: Springer.

Kattan, N., Thome, J. R., & Favrat, D. (1998). Flow boiling in horizontal tubes: Part 1 - development of a diabatic two-phase flow pattern map [Journal Article]. *Journal of Heat Transfer-Transactions of the Asme*, *120*(1), 140-147.

Konishi, C., & Mudawar, I. (2015). Review of flow boiling and critical heat flux in microgravity. *International Journal of Heat and Mass Transfer*, *80*(0), 469-493.

Luchinsky, D. G., Smelyanskiy, V. N., & Brown, B. (2014a). *Physics based model for cryogenic chilldown and loading. part i: Algorithm* (Technical Publication No. NASA/TP-2014-216659). NASA, ARC.

Luchinsky, D. G., Smelyanskiy, V. N., & Brown, B. (2014b). *Physics based model for cryogenic chilldown and loading. part ii: Verification and validation* (Technical Publication No. NASA/TP-2014-218298). NASA, ARC.

Luchinsky, D. G., Smelyanskiy, V. N., & Brown, B. (2014c). *Physics based model for cryogenic chilldown and loading. part iv: Code structure* (Technical Publication No. NASA/TP-2014-218399). NASA, ARC.

Nellis, G., & Klein, S. (2009). *Heat transfer* [Book]. Cambridge University Press.

Nourgaliev, R., & Christon, M. (2012). *Solution algorithms for multi-fluid-flow averaged equations* (Technical Report No. INL/EXT-12-27187). Idaho, US.

Prosperetti, A., & Tryggvason, G. (2007). *Computational methods for multiphase flow* [Book]. Cambridge University Press.

RELAP5:1. (2012). Relap5-3d code manual volume **I**: Code structure, system models, and solution methods (Computer software manual No. INEEL-EXT-98-

00834). INEL.

RELAP5:4. (2012). Relap5-3d code manual volume iv: Models and correlations (Computer software manual No. INEEL-EXT-98-00834).

Robert, J., William, N., Kelly, C., & Evelyn, O.-S. (2012). Integrated ground operations demonstration units testing plans and status [Book Section]. In *Aiaa space 2012 conference & exposition.* American Institute of Aeronautics and Astronautics.

Staedtke, H. (2006). *Gasdynamic aspects of two-phase flow: Hyperbolicity, wave propagation phenomena and related numerical methods*. Wiley.

Steiner, D., & Kind, M. (2010). Vdi heat atlas. In V.-G. V. u. Chemieingenieurwesen & V. Gesellschaft (Eds.), (2nd ed., pp. 796–800). Heidelberg: Springer-Verlag.

Tong, L. S., & Tang, Y. S. (1997). *Boiling heat transfer and two-phase flow* [Book]. Taylor & Francis.

TRACE5. (2007). Trace v5.0 theory manual field equations, solution methods, and physical models [Computer software manual].

Wallis, G. B. (1969). *One-dimensional two-phase flow* [Book]. McGraw-Hill.

Wojtan, L., Ursenbacher, T., & Thome, J. R. (2005). Investigation of flow boiling in horizontal tubes: Part i - a new diabatic two-phase flow pattern map [Journal Article]. *International Journal of Heat and Mass Transfer*, *48*(14), 2955-2969.

Zeldovich, Y. (1970). Gravitational instability: An Approximate theory for large density perturbations. *Astron.Astrophys.*, *5*, 84-89.

Zuber, N., & Tribus, M. (1958). *Further remarks on the stability of boiling* (Report No. 58-5). UCLA.

BIOGRAPHIES

Dmitry G. Luchinsky is a senior research scientist in MCT Inc. He obtained his MSc and PhD in physics in Moscow working on nonlinear optics of semiconductors. He is an author of more than 100 publications. He has been on a number of occasions a Royal Society Visiting Fellow and a NASA visiting scientist. He worked as a senior scientific researcher in VNII for Metrological Service (Moscow, Russia) and as a Senior Research Fellow in Lancaster University (Lancaster, UK). His research interests include nonlinear optics, stochastic and chaotic nonlinear dynamics, dynamical inference, fluid dynamics, ionic motion. His research is currently focused on theory and CFD of gas dynamics and cryogenic flows.

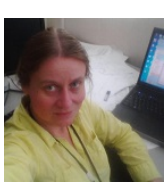

Ekaterina Ponizovskaya-Devine Dr. Ekaterina Ponizovskaya-Devine is a research scientist in SGT since 2009. Her current work is related to integrated health management and control of cryogenic propellant loading systems and two-phase cryogenic flow modeling. She obtained her PhD at Moscow institute of Physics and Technology in Physics, working on stochastic resonance in non-equilibrium electron-hole plasma. She was a post-doc in Spanish National Research Council, working in photonics, nanotechnology, negative index materials. In 2005 she had Visiting Scholar position at HP Lab working in nanotechnology. Her research interests are physics based models, two-phase flow, nanotechnology, physics model based fault diagnostics, optimization and control. .

Michael Khasin Dr Michael Khasin is a Senior Researcher in SGT Inc., working at NASA Ames Research Center. He holds B.Sc. in Physics (Honors Program), 2001, M.Sc. in physics, 2003, and PhD in chemical physics, 2008, from the Hebrew University of Jerusalem. As a postdoctoral researcher at Michigan State University, Massachusetts Institute of Technology, and University of Michigan, Michael worked on the theory of non-equilibrium systems and their control and transport in disordered system. His research interests include applied physics, nonlinear and stochastic dynamics, large fluctuations and their control in non-equilibrium systems and efficient simulation of complex dynamics. He has been an invited speaker to many international and national conferences and workshops. Currently his research is focused on the theory of heat transfer, fluid dynamics, and fluid structure interaction.

Dŏgan A. Timuçin is a Research Scientist in the Intelligent Systems Division at NASA Ames Research Center. He holds B.S. (1989), M.S. (1991), and Ph.D. (1994) degrees in electrical engineering, and has been with NASA since 1995. His research interests are in the general areas of classical electrodynamics and optics, statistical physics, nonlinear dynamics, Bayesian inference, and numerical optimization.

APPENDIX A

the elements of the matrix A_x^n can be written in the following form (index (j) enumerates columns of the matrix A_x^n)

$$A_x^{(1)} = \begin{bmatrix} \alpha_{g,L}^n \left(\partial_e \rho\right)_{g,L}^n \\ \alpha_{g,L}^n \left(\left(e\partial_e \rho\right)_{g,L}^n + \rho_{g,L}^n\right) \\ 0 \\ \alpha_{g,L}^n \left(\partial_e \rho\right)_{g,L}^n \end{bmatrix};$$

$$A_x^{(2)} = \begin{bmatrix} -\beta_{g,L}^n \left(\partial_e \rho\right)_{l,L}^n \\ 0 \\ \beta_{g,L}^n \left(\rho_{l,L}^n + \left(e\partial_e \rho\right)_{l,L}^n\right) \\ \beta_{g,L}^n \left(\partial_e \rho\right)_{l,L}^n \end{bmatrix}$$

$$A_x^{(3)} = \begin{bmatrix} \rho_{g,L}^n + \rho_{l,L}^n \\ \left(e\rho\right)_{g,L}^n + p_L^n \\ -\left(e\rho\right)_{l,L}^n - p_L^n \\ \rho_{g,L}^n - \rho_{l,L}^n \end{bmatrix};$$

$$A_x^{(4)} = \begin{bmatrix} \alpha_{g,L}^n \left(\partial_p \rho\right)_{g,L}^n - \beta_{g,L}^n \left(\partial_p \rho\right)_{l,L}^n \\ \left(e\alpha\partial_p \rho\right)_{g,L}^n \\ \left(\beta e\partial_p \rho\right)_{l,L}^n \\ \alpha_{g,L}^n \left(\partial_p \rho\right)_{g,L}^n + \beta_{g,L}^n \left(\partial_p \rho\right)_{l,L}^n \end{bmatrix}$$

Columns of the vector-multipliers for gas velocities on the

right hand side of the eq. (8) have the form

$$a_x^n = -\begin{bmatrix} \widehat{\rho}^n_{g,j+1} \\ \left(\widehat{e}\,\widehat{\rho}\right)^n_{g,j+1} + p^n_L \\ 0 \\ \widehat{\rho}^n_{g,j+1} \end{bmatrix} \cdot n^n_{g,j+1};$$

$$b_x^n = \begin{bmatrix} \widehat{\rho}^n_{g,j} \\ \left(\widehat{e}\,\widehat{\rho}\right)^n_{g,j} + p^n_L \\ 0 \\ \widehat{\rho}^n_{g,j} \end{bmatrix} \cdot n^n_{g,j};$$

Vector-columns for the liquid velocities are

$$c_x^n = \begin{bmatrix} \widehat{\rho}^n_{l,j+1} \\ 0 \\ -\left(\widehat{e}\,\widehat{\rho}\right)^n_{l,j+1} - p^n_L \\ -\widehat{\rho}^n_{l,j+1} \end{bmatrix} \cdot n^n_{l,j+1};$$

$$d_x^n = \begin{bmatrix} -\widehat{\rho}^n_{l,j} \\ 0 \\ \left(\widehat{e}\,\widehat{\rho}\right)^n_{l,j} + p^n_L \\ \widehat{\rho}^n_{l,j} \end{bmatrix} \cdot n^n_{l,j},$$

where the coefficients $n^n_{i,j}$ are of the form

$$n^n_{g,j} = \widehat{\alpha}^n_{g,j}\frac{\Delta t A_j}{V_L}; \quad n^n_{l,j} = \widehat{\alpha}^n_{l,j}\frac{\Delta t A_j}{V_L}.$$

Finally, the free vector in eq. (8) is written as follows

$$e_x^n = \begin{bmatrix} 2\Gamma^n_{g,L}V_L \\ \Gamma^n_{g,L}H^n_{wg}V_L - Q_{wg} \\ -\Gamma^n_{g,L}H^n_{wl}V_L - Q_{wl} \\ 0 \end{bmatrix} \cdot \tfrac{\Delta t}{V_L} + a^n_x u^n_{g,j+1} + b^n_x u^n_{g,j} + c^n_x u^n_{l,j+1} + d^n_x u^n_{l,j}$$

APPENDIX B

The equations for velocities solved in the nearly-implicit algorithm have the following form (RELAP5:1, 2012)

$$\begin{aligned} &\alpha\rho_g u_{g,t} + \beta\rho_l u_{l,t} + \tfrac{\alpha\rho_g}{2}\left(u_g^2\right)_{,x} + \tfrac{\beta\rho_l}{2}\left(u_l^2\right)_{,x} + p_{,x} = \\ &\quad -\rho_m z_{,x} - \rho_g u_g F_{wg} - \beta\rho_l u_l F_{wl} - \Gamma_g\left(u_g - u_l\right), \\ &u_{g,t} - u_{l,t} + \tfrac{\left(u_g^2\right)_{,x}}{2} + \tfrac{\left(u_l^2\right)_{,x}}{2} + \left(\tfrac{1}{\rho_g} + \tfrac{1}{\rho_l}\right)p_{,x} = \\ &\quad u_l F_{wl} - u_g F_{wg} + \tfrac{\Gamma_g}{\alpha\rho_g}\left(u_i - u_g\right) + \tfrac{\Gamma_g}{\beta\rho_l}\left(u_i - u_l\right) + \\ &\quad \rho_m F_i\left(u_g - u_l\right) + \tfrac{\rho_m}{\alpha\rho_g\beta\rho_l}\tilde{M}_V \end{aligned}$$

Applying equation (9) to momenta equations in (1) and (2) we obtain the explicit form of the matrix coefficients in (10) given below. For the coefficients of the A_i matrix

$$\begin{aligned} a^n_{k,11} &= \left(-(\widetilde{\alpha\rho})^n_{g,j}\,(b\cdot u)^n_{g,L-1} - a_{p2,L-1}\right)\Delta t; \\ a^n_{k,12} &= \left(-(\widetilde{\alpha\rho})^2_{l,j}\,(b\cdot u)^n_{l,L-1} - a_{p4,L-1}\right)\Delta t \\ a^n_{k,21} &= \left(\left(\tfrac{\widetilde{\alpha\rho}}{\overline{\alpha\rho}}\right)^n_{g,j}(b\cdot u)^n_{g,L-1} - \left(\tfrac{\bar\rho_l - \bar\rho_g}{\bar\rho_l\bar\rho_g}\right)a_{p2,L-1}\right)\Delta t; \\ a^n_{k,22} &= \left(\left(\tfrac{\widetilde{\alpha\rho}}{\overline{\alpha\rho}}\right)^n_{l,j}(b\cdot u)^n_{l,L-1} - \left(\tfrac{\bar\rho_l - \bar\rho_g}{\bar\rho_l\bar\rho_g}\right)a_{p4,L-1}\right)\Delta t. \end{aligned}$$

For the coefficients of the B_i matrix we have

$$\begin{aligned} b^n_{k,11} &= \left(\left((\overline{\alpha\rho})^n_{g,j}\left(1 + F^n_{wg,j}\right) + \Gamma^n_{g,j}\right)\Delta x_j + (\widetilde{\alpha\rho})^n_{g,j} \times \right. \\ &\quad \left.\left((b\cdot u)^n_{g,L} - (a\cdot u)^n_{g,L-1}\right) + \left(a_{p2,L} - a_{p1,L-1}\right)\right)\Delta t; \\ b^n_{k,12} &= \left(\left((\overline{\alpha\rho})^n_{l,j}\left(1 + F^n_{wl,j}\right) - \Gamma^n_{g,j}\right)\Delta x_j + (\widetilde{\alpha\rho})^n_{l,j} \times \right. \\ &\quad \left.\left((b\cdot u)^n_{l,L} - (a\cdot u)^n_{l,L-1}\right) + \left(a_{p4,L} - a_{p3,L-1}\right)\right)\Delta t; \end{aligned}$$

$$\begin{aligned} \tfrac{b^n_{k,21}}{\Delta t} &= \left(\tfrac{\widetilde{\alpha\rho}}{\overline{\alpha\rho}}\right)^n_{g,j}\left((b\,u)^n_{g,L} - (a\,u)^n_{l,L-1}\right) + F^n_{wg,j}\Delta x_j \\ &+ \left(1 + \tfrac{c(\bar\rho^n_m)^2}{\bar\rho^n_g\bar\rho^n_l}\right)_j \tfrac{\Delta x_j}{\Delta t} - \tfrac{\Gamma^n_{g,j}}{(\overline{\alpha\rho})^n_{g,j}}\left(\tfrac{\lambda^n_j\bar\rho^n_{m,j}}{(\overline{\alpha\rho})^n_{l,j}} - 1\right)\Delta x_j \\ &\quad + \left(\tfrac{\bar\rho_l - \bar\rho_g}{\bar\rho_l\bar\rho_g}\right)\left(a_{p2,L} - a_{p1,L-1}\right) + \bar\rho^n_{m,j}F^n_{i,j}\Delta x_j; \end{aligned}$$

$$\begin{aligned} \tfrac{b^n_{k,22}}{\Delta t} &= -\left(\tfrac{\widetilde{\alpha\rho}}{\overline{\alpha\rho}}\right)^n_{l,j}\left((b\,u)^n_{l,L} - (a\,u)^n_{l,L-1}\right) - F^n_{wl,j}\Delta x_j \\ &- \tfrac{\Gamma^n_{g,j}}{(\overline{\alpha\rho})^n_{l,j}}\left(\tfrac{\left(1-\lambda^n_j\right)\bar\rho^n_{m,j}}{(\overline{\alpha\rho})^n_{g,j}} - 1\right)\Delta x_j - \left(1 + \tfrac{c(\bar\rho^n_m)^2}{\bar\rho^n_g\bar\rho^n_l}\right)_j \tfrac{\Delta x_j}{\Delta t} \\ &\quad \left(\tfrac{\bar\rho_l - \bar\rho_g}{\bar\rho_l\bar\rho_g}\right)\left(a_{p4,L} - a_{p3,L-1}\right) - \bar\rho^n_{m,j}F^n_{i,j}\Delta x_j; \end{aligned}$$

For the coefficients of C_i matrices we have

$$\begin{aligned} c^n_{k,11} &= \left((\widetilde{\alpha\rho})^n_{g,j}\,a_{g,L}u^n_{g,L} + a_{p1,L}\right)\Delta t; \\ c^n_{k,12} &= \left((\widetilde{\alpha\rho})^n_{l,j}\,a_{l,L}u^n_{l,L} + a_{p3,L}\right)\Delta t; \\ c^n_{k,21} &= \left(\left(\tfrac{\widetilde{\alpha\rho}}{\overline{\alpha\rho}}\right)^n_{g,j}a_{g,L}u^n_{g,L} + \left(\tfrac{\bar\rho_l - \bar\rho_g}{\bar\rho_l\bar\rho_g}\right)a_{p1,L}\right)\Delta t; \\ c^n_{k,22} &= \left(-\left(\tfrac{\widetilde{\alpha\rho}}{\overline{\alpha\rho}}\right)^n_{g,j}a_{l,L}u^n_{l,L} + \left(\tfrac{\bar\rho_l - \bar\rho_g}{\bar\rho_l\bar\rho_g}\right)a_{p3,L}\right)\Delta t. \end{aligned}$$

The free vector has the form

$$\begin{aligned} \tfrac{n^n_{2k}}{\Delta t} &= \bar\rho^n_{m,j}g\left(\tfrac{\bar\rho_l - \bar\rho_g}{\bar\rho_l\bar\rho_g}\right)\Delta y^n_L - \tfrac{(\overline{\alpha\rho})^n_{g,j}}{2}\left(u^2_L - u^2_{L-1}\right)^n_g \\ &+ \tfrac{(\overline{\alpha\rho})^n_{l,j}}{2}\left(\left(u^n_{l,L}\right)^2 - \left(u^n_{l,L-1}\right)^2\right) + \left[\tfrac{\Gamma_g\bar\rho_m}{(\overline{\alpha\rho})_g(\overline{\alpha\rho})_l} \times \right. \\ &\left.\left(\lambda u_g - (1-\lambda)\,u_l\right) - \tfrac{\Gamma_g}{(\overline{\alpha\rho})_g}u_g - \tfrac{\Gamma_g}{(\overline{\alpha\rho})_l}u_l\right]^n_j \Delta x_j - \\ &\left(F_{wg}u_g - F_{wl}u_l\right)^n_j\Delta x_j - \left(\tfrac{\bar\rho_l - \bar\rho_g}{\bar\rho_l\bar\rho_g}\right) \times \\ &\left(p + a_{p5}\right)^n_L - \left(p - a_{p5}\right)^n_{L-1} - \left(\bar\rho_m F_i\left(u_g - u_l\right)\right)^n_j\Delta x_j; \end{aligned}$$

$$\begin{aligned} \tfrac{n^n_{2k+1}}{\Delta t} &= -\left(-\bar\rho^n_{m,j}g\Delta z_j + (\widetilde{\alpha\rho}F_w u)^n_{g,j} + \left(\widetilde{\alpha\rho}F_w u\right)^n_{l,j} + \right. \\ &\left.\Gamma_g\left(u_g - u_l\right)^n_j\right)\Delta x_j - \left(\tfrac{(\overline{\alpha\rho})_j}{2}\left(u^2_L - u^2_{L-1}\right)\right)^n_g - \\ &\left(\tfrac{(\overline{\alpha\rho})_j}{2}\left(u^2_L - u^2_{L-1}\right)\right)^n_l - (p + a_{p5})^n_L + (p - a_{p5})^n_{L-1}; \end{aligned}$$

APPENDIX C

The unexpanded equations of the energy and mass conservation have the same structure (11). We have for gas density

$$dU_L^{n+1} = d\left(\alpha\rho\right)_{g,L}^{n+1},$$
$$S_{g,L} = \tilde{\Gamma}_{g,L}^{n}\Delta t - \left(\alpha\rho\right)_{g,j+1}^{n}\gamma_{g,j+1}^{n+1} + \left(\alpha\rho\right)_{g,j}^{n}\gamma_{g,j}^{n+1},$$

for liquid density $dU_L^{n+1} = d\left(\alpha\rho\right)_{l,L}^{n+1}$

$$S_L = -\tilde{\Gamma}_{g,L}^{n}\Delta t - \left(\alpha\rho\right)_{l,j+1}^{n}\gamma_{l,j+1}^{n+1} + \left(\alpha\rho\right)_{l,j}^{n}\gamma_{l,j}^{n+1},$$

for gas energy $dU_L^{n+1} = d\left(\alpha\rho e\right)_{g,L}^{n+1}$

$$S_L = \left(\left(\alpha\rho e\right)_{g,j+1}^{n} + \left(\alpha\rho\right)_{g,j+1}^{n} p_L^{n+1}\right)\gamma_{g,j+1}^{n+1} - \left(\left(\alpha\rho e\right)_{g,j}^{n} + \left(\alpha\rho\right)_{g,j}^{n} p_L^{n+1}\right)\gamma_{g,j}^{n+1} - p_L^n d\tilde{\alpha}_{g,L}^{n} + \left(\dot{q}_{wg}\frac{S_{wg}}{V} + \dot{q}_{ig}\frac{S_{ig}}{V} + \tilde{\Gamma}_{wg}\tilde{h}_{wg} + \tilde{\Gamma}_{ig}\tilde{h}_{ig}\right)_L^n \Delta t,$$

and for the liquid energy $dU_L^{n+1} = d\left(\alpha\rho e\right)_{l,L}^{n+1}$

$$S_L = \left(\left(\alpha\rho e\right)_{l,j+1}^{n} + \left(\alpha\rho\right)_{l,j+1}^{n} p_L^{n+1}\right)\gamma_{l,j+1}^{n+1} - \left(\left(\alpha\rho e\right)_{g,j}^{n} + \left(\alpha\rho\right)_{l,j}^{n} p_L^{n+1}\right)\gamma_{l,j}^{n+1} + p_L^n d\tilde{\alpha}_{g,L}^{n} + \left(\dot{q}_{wl}\frac{S_{wl}}{V} + \dot{q}_{il}\frac{S_i}{V} - \tilde{\Gamma}_{wg}\tilde{h}_{wg} - \tilde{\Gamma}_{ig}\tilde{h}_{ig}\right)_L^n \Delta t$$

Coefficients $\lambda_j^{(n+1)}$ and $\mu_j^{(n+1)}$ given by the expressions for upwind values for densities

$$\tilde{\lambda}_j^{n+1} = 1 + \left(s_{u,j} + z_{u,j}\cdot s_{p,j}\right),$$
$$\tilde{\mu}_j^{n+1} = 1 - \left(s_{u,j} + z_{u,j}\cdot s_{p,j}\right),$$

and energies

$$\lambda_j^{n+1} = \tilde{\lambda}_j^{n+1} - z_{u,j}z_{p,j}\frac{\rho_{g(l),L} - \rho_{g(l),L-1}}{\rho_{g(l),L-1} + \rho_{g(l),L}},$$
$$\mu_j^{n+1} = \tilde{\mu}_j^{n+1} + z_{u,j}z_{p,j}\frac{\rho_{g(l),L} - \rho_{g(l),L-1}}{\rho_{g(l),L-1} + \rho_{g(l),L}}.$$